

# 3D Printed SERS-Active Thin-Film Substrates Used to Quantify Levels of the Genotoxic Isothiazolinone

Siddhant Jaitpal, Suhash Reddy Chavva, and Samuel Mabbott\*

Cite This: *ACS Omega* 2022, 7, 2850–2860

Read Online

ACCESS |



Metrics &amp; More

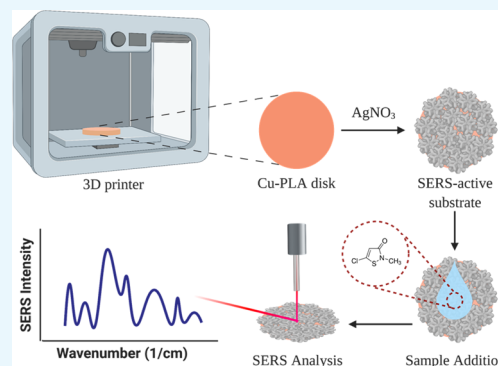


Article Recommendations



Supporting Information

**ABSTRACT:** Several reports present methods to fabricate thin-film substrates capable of surface-enhanced Raman scattering (SERS). Substrates synthesized by displacing silver onto copper using facile synthesis methods such as galvanic displacement can generate high levels of SERS enhancement rivaling commercially available substrates manufactured by lithographic methods. Here, we describe the optimization of a novel set of SERS-active thin-film substrates synthesized via the electroless displacement of Ag onto the surface of three-dimensional (3D) printed disks composed of the copper/polymer (PLA) composite filament. The effect of  $\text{AgNO}_3$  concentration on the deposition, morphology, and overall SERS activity of the substrates has been carefully studied. Two commonly used Raman reporters, 4-mercaptobenzoic acid (MBA) and malachite green isothiocyanate (MGITC), were used to measure the SERS output of the substrates. Good SERS signal reproducibility (RSD  $\sim 16.8\%$ ) was measured across the surface of replicate substrates and high-sensitivity detection of MBA was achieved ( $10^{-12}$  M). To test the real-world application of our substrates, we opted to detect 5-chloro-2-methyl-4-isothiazolin-3-one (CMIT), which is a genotoxic, biocide common in many household products, known to leach into water supplies. Our newly developed SERS-active substrates could detect CMIT down to 10 ppm when spiked in simulated lake water samples, which is well within current agency standards.



## INTRODUCTION

SERS is a highly sensitive analytical tool capable of significantly enhancing the Raman scattering observed from analytes of interest. This advanced spectroscopic technique has been applied across a range of scientific disciplines including analytical chemistry, diagnostics, and environmental analysis.<sup>1</sup> Researchers have shown that SERS can detect analytes of interest at the attomole level while allowing seamless identification and differentiation of inorganic/organic contaminants, nanomaterials, and pathogens contained within environmental samples.<sup>2</sup> The two mechanisms associated with SERS are chemical enhancement, which relies on charge transfer between the analyte and the material and electromagnetic enhancement (EM), which is the second mode and is the strongest. This consists of plasmon excitation close to the surface of the metal substrate.<sup>3,4</sup> The metallic substrates typically demonstrate a strong localized surface plasmon resonance, which facilitates strong electromagnetic (EM) field enhancement of Raman signals associated with analytes adsorbed or located near these plasmonic materials. A highly localized region of electric field occurring between nanostructures is termed a plasmonic “hotspot”.<sup>5</sup> SERS-active substrates are typically made from nanostructured gold, silver, or copper.<sup>6</sup>

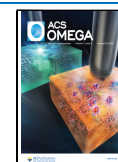
SERS substrates can be loosely placed into two general categories: (i) nanoparticle suspensions (sols) and (ii) metal nanostructures comprising a thin-film substrate. While nanoparticle sols possess inherent simplicity in their direct

application (pipetting/mixing and analyzing), drawbacks include inhomogeneity arising from nonuniform particle size and difficulty controlling the required nanoparticle aggregation, which can lead to imprecise hotspot generation. These issues negatively affect the reproducibility of SERS measurements, contributing to their diminished potential for widespread use. Solid, SERS-active thin-film platforms can be manufactured using a variety of fabrication methods including top-down and bottom-up lithographic methods or combinations of both. However, while these fabrication methods might offer a relative improvement in the homogeneity of the SERS signal, they are often cost-prohibitive, requiring advanced manufacturing facilities.<sup>7,8</sup> To that end, novel facile methods toward the development of thin-film SERS substrates have been developed; notably, Xu et al. developed laser-induced plasma-assisted ablation (LIPAA) to fabricate thin films for in situ SERS for food safety applications.<sup>9</sup> Zhou et al. developed a flexible polyethylene (PE) transparent film on which a silver nanocube monolayer was deposited. This film

Received: October 12, 2021

Accepted: December 29, 2021

Published: January 10, 2022



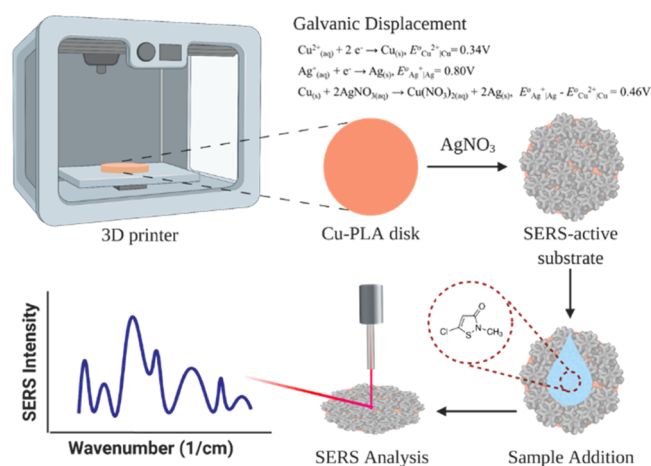
was cut-pasted onto fruits to perform SERS analysis to monitor toxic pesticide levels.<sup>10</sup> Additionally, Chen et al. developed a green synthesis method for the large-scale fabrication of the nanoporous Au nanorod with an ultrathin Ag-layer in situ electrodeposited on each nanoporous Au nanorod. Multiplexed SERS detection of nonadsorbing environmental contaminants polychlorinated biphenyl (PCB) and Raman probe R6G was possible through a monolayer modification with thiol-cyclodextrin.<sup>11</sup> Hence, there is still a critical need for simple fabrication methods, which utilize minimal advanced equipment and can be readily deployed by cross-disciplinary scientific teams. The need of the hour is to manufacture simple, low-cost SERS-active substrate preparation methods, which include inkjet printing, screen printing, and galvanic displacement. All of these techniques have been applied to the detection of trace chemical and biological species and are compatible with large-scale fabrication.<sup>12</sup>

Interest in three-dimensional (3D) printing or additive manufacturing has grown rapidly over the past decade. In its simplest form, controlled layer-by-layer deposition of materials is exploited to generate physical objects according to predefined 3D models. Some specific advantages include rapid iterative development by modification of geometric, structural, and/or compositional design, elimination of time-consuming tooling, engineering, and ultimately minimal waste material generation. Analytical chemistry labs are working toward developing ingenious uses for the technology looking beyond standard prototyping. The consensus appears to be moving toward printing functional devices imbued with electroactive, catalytic functionality for use in sensing applications.<sup>13–16</sup> Fused deposition modeling (FDM) is the most widely used additive manufacturing method due to its low-cost, extensive hardware availability with widely ranging thermoplastic polymer filaments. Fabrication of electronic components including sensors has been demonstrated using metal/polymer composites composed of magnetic/electrically active fillers,<sup>17,18</sup> whereby the compositions of metal/polymer matrices are adjusted to overcome challenges with reduced thermal and electrical conductivity.<sup>19</sup> Plating methods like electroless deposition (also known as galvanic displacement) or electroplating have been applied as finishing treatments to thermoplastic polymers for improved electromechanical properties.<sup>20</sup> The combination of electroplating and 3D printing methods such as FDM allows for the generation of geometrically and electrically functional structures. Electroless deposition does not require the application of external current; instead, it utilizes the metal's position in the electrochemical series. A metal with a greater positive redox potential (plating solution) is capable of displacing metals with lower redox potentials. The plating process is achieved via a spontaneous, thermodynamically favorable reaction. The process can continue indefinitely till the dissolution of the sacrificial anode (metal with less positive redox potential) is complete, with additional chemical reducing agents often being added as the source of electrons.<sup>21</sup> Exploiting electroless deposition to create SERS-active substrates is attractive due to their facile fabrication procedure. Electroless deposition is diffusion-limited, meaning the size of deposited structures is directly related to the size of the less noble metal on the surface.<sup>22</sup> It has demonstrated great utility in the fabrication of high enhancement factor SERS substrates.<sup>23–25</sup>

FDM printing yields thin layer-by-layer anisotropic structures that extend to their physical properties, which

have been studied in the following domains: mechanical,<sup>26</sup> magnetic,<sup>27</sup> thermal,<sup>28</sup> and electrical.<sup>29</sup> Anisotropy has been leveraged toward the generation of stable hotspots and plasmonic tunability in metal nanoparticles using shapes such as rods, triangles, prisms, cubes, and stars.<sup>30</sup> These shapes have shown tremendous potential in SERS-based sensing and imaging. Anisotropic silver nanostructures have been studied extensively for EM-based SERS enhancement, which is postulated to proceed via “hotspots” generated at their peripheries. Their high surface area leaves them prone to oxidation<sup>31</sup> and corrosion by sulfides,<sup>32</sup> which effectively decrease the Raman scattering cross-section, thus affecting SERS performance. On the other hand, anisotropic silver microstructures are more chemically stable and have been demonstrated to exhibit great SERS performance.<sup>33,34</sup> In this report, we use FDM-based 3D printing to fabricate copper-poly(lactic acid) (Cu-PLA) disks followed by the growth of anisotropic silver microstructures via galvanic displacement. The effect of silver microstructure dimensions and shapes on the resultant SERS signal was investigated and the reproducibility of the signal was analyzed (Scheme 1). As a proof of

**Scheme 1. FDM 3D Printing Workflow Demonstrates the Fabrication of the Cu-PLA Discs Followed by Galvanic Displacement, Sample Addition, and SERS Measurement with Constitutive Galvanic Half-Cell Equations, which Facilitate Deposition of Ag Microstructures on Cu-PLA**



concept, to demonstrate the efficacy of 3D printed substrates, we also demonstrate the utility of the silver-coated polymer disks toward biosensing of biocide 5-chloro-2-methyl-4-isothiazolin-3-one (CMIT) at concentrations set forth by environmental regulatory agencies. To our knowledge, this is the first report combining FDM-based 3D printing and galvanic displacement for quantitative SERS sensing.

## RESULTS AND DISCUSSION

**SEM Characterization with EDS Mapping.** Electroless deposition/galvanic displacement was used to prepare SERS-active silver structures. The process occurs via a redox reaction where the copper embedded in the PLA matrix is oxidized in the presence of silver ions. The displacement reaction yields final structures with a variety of distinct morphologies including dendritic shapes and jagged-edged polyhedral crystals that have been known to aid SERS enhancement (eq 1). The silver ions are adsorbed on the area of embedded

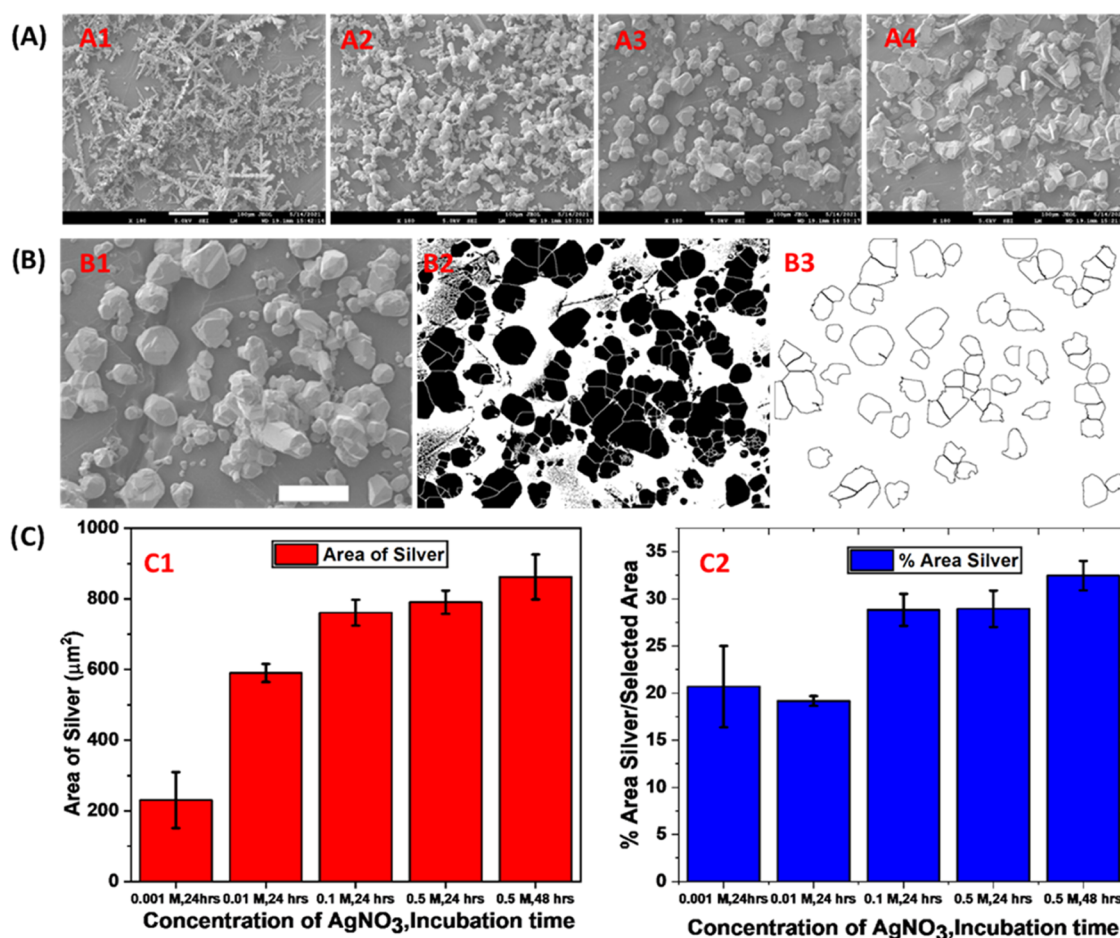
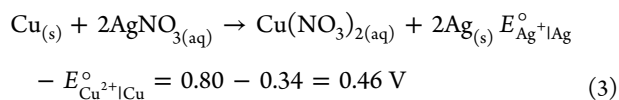
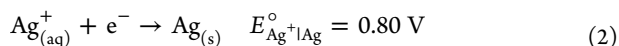
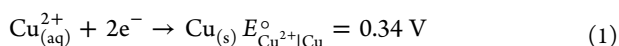


**Figure 1.** (A) SEM images demonstrating the effect of silver concentration on the size and coverage of polyhedral silver structures ((A1–A4), 0.001, 0.01, 0.1, and 0.5 M), scale bars = 100  $\mu\text{m}$ . (B) Thresholding and segmentation of the image were used to calculate the area of polyhedral silver crystals and total surface area coverage (B1: image, B2: local thresholding and watershed, B3: segmented image for analysis), scale bars = 25  $\mu\text{m}$ . (C) Histograms displaying the average area of polyhedral silver crystals on the Cu–PLA disk (C1) and the % silver occupying the disk surface (C2). Error bars represent the standard deviation calculated across 5 measured areas on disks.

copper and are further reduced to form silver microstructures (Figure 1). The reaction of  $\text{AgNO}_3$  solution and sacrificial embedded copper is spontaneous and given by a positive redox potential ( $E^\circ$ ) and is displayed in eqs 1–3



Ag–Cu–PLA disks incubated for 24 h were analyzed using SEM. Distinct morphological changes were associated with increased  $\text{AgNO}_3$  concentration. Fine micron-sized fractal dendrites can be observed at the lowest concentration (0.001 M, Figure 1A-A1). These micron-sized dendritic structures possess a large surface-area-to-volume ratio and have been known to create several “hotspots” capable of significant SERS enhancement effects. These are supported by theoretical calculations confirming confined electromagnetic enhancement at the sharp protrusions of these structures.<sup>35,36</sup> The growth of silver structures on the Cu–PLA substrate can be explained by the diffusion-limited aggregation theory (DLA), which defines

the fast-kinetic galvanic displacement process as being diffusion-limited. The reduction of silver ions in the solution results in nucleation-based growth. Disk-shaped nanoplate structures are formed due to the parallel growth of the  $\langle 1,1,1 \rangle$  stacking fault planes.<sup>37</sup> The stacking faults serve as secondary nucleation sites where  $\text{Ag}^+$  ions are further reduced. These sites upon depletion of  $\text{Ag}^+$  ions result in the formation of dendrite-like structures. Thus, diffusion and availability of  $\text{Ag}^+$  ions affect dendrite formation.<sup>25,37,38</sup> An increase in the  $\text{AgNO}_3$  concentration to 0.01 M reveals the formation of globular deposits on the existing branches of the dendritic structures (Figure 1A-A2). Further increase in the  $\text{AgNO}_3$  concentration (0.1 and 0.5 M, Figure 1A-A3,A4, respectively) reveals that the deposits become more globular, and at 0.5 M, distinct jagged-edged polyhedrals are formed on the surface of the disks, which show a lack of sharp tips. The excess availability of  $\text{Ag}^+$  ions results in the formation of polyhedral silver structures reducing the amount of the exposed PLA matrix. Some studies reveal that these large structures demonstrate reduced SERS efficiency when used as a nanocomposite.<sup>39</sup> Previous studies of the galvanic displacement of silver onto copper have shown that inherently present fluoride, sulfate, and chloride anions influence the formation of metal micro/nanostructures without actual incorporation into the structure.<sup>38,40,41</sup> However, aggregation-driven growth from smaller dendritic to larger

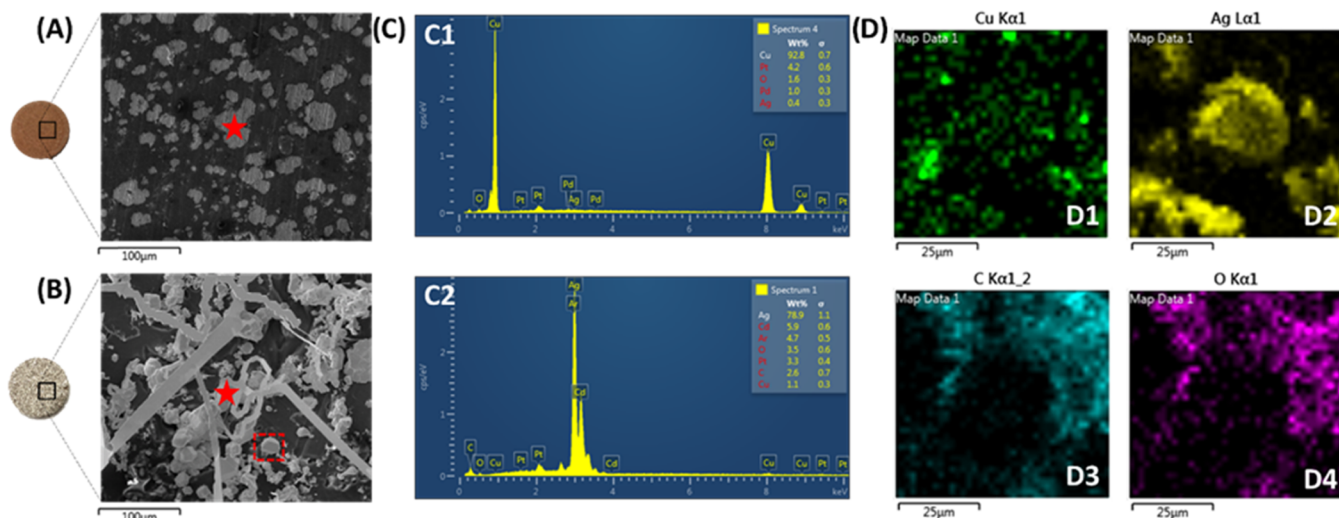


**Figure 2.** Optical and SEM images used to evaluate the success of electroless deposition of silver on the Cu–LA disk are shown (A, B). The SEM images show the surface of the control Cu–PLA disk (A) and Ag–Cu–PLA disk (0.1 M AgNO<sub>3</sub>, 24 h incubation) (B). (C) Results of the EDS analysis used to understand the elemental composition of the Cu–PLA and Ag–Cu–PLA disks. Red stars on the SEM images (A, B) indicate the points at which EDS spectra were collected. Cu (C1) and silver (C2) are the dominant peaks observed on the Cu–PLA and Ag–Cu–PLA substrates, respectively. (D) Elemental maps of the Ag–Cu–PLA substrate collected from the area indicated by the dashed red box area present in the SEM image (B). Representative elements include copper (green, D1), silver (yellow, D2) with carbon (cyan, D3) and oxygen (magenta, D4).

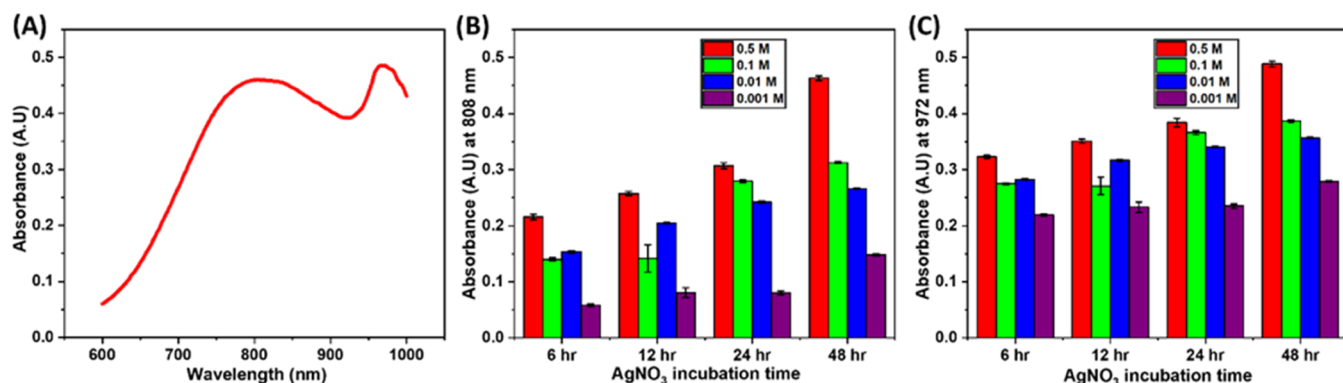


**Figure 3.** (A) Example of the extinction spectra representative of the Cu<sup>2+</sup> ions (when using 0.1 M AgNO<sub>3</sub>, 24 h incubation) displaced after galvanic displacement was performed. (B, C) Histograms created from measuring the peak maxima of the absorbance bands representative of the concentration of Cu<sup>2+</sup> ions displaced in solution.

polyhedral crystals could be explained by the lack of these stabilizing ions in the displacement solution. Due to their relatively small size, they have been known to accumulate at sites of nucleation and stabilize against aggregation via electrostatic interaction.<sup>38,42</sup>

Using ImageJ software, the SEM images were analyzed to determine the effect of AgNO<sub>3</sub> concentration on the size and distribution of silver deposits across the surface of the disks. SEM images of 0.1 M AgNO<sub>3</sub> with an incubation time of 24 h (Figure 1B–B1) were used to demonstrate thresholding (Figure 1B–B1) and segmentation (Figure 1B–B2) to quantify morphological differences in terms of displaced silver for different AgNO<sub>3</sub> concentrations at endpoints of 24 and 48 h. The diffusion-limited aspect of silver growth on the disk was verified by analyzing the average size of the silver crystals (Figure 1C–C1) and the percentage surface area coverage (Figure 1C–C2). In both cases, an increase in the polyhedral crystal area and deposition area is observed. The increase in the average silver crystal size and silver deposition area appears to saturate at the 0.1 M AgNO<sub>3</sub>, 24 h condition with minimal

increases observed at 0.5 M, 48 h (highest assayed concentration). Thus, the 24 h incubation time appears to be important considering the diffusion-limited aspect of the galvanic displacement for the dimensions of disks used in our study.

Optical images of the disks before (control, Figure 2A, left) and after submerging in 0.1 M AgNO<sub>3</sub> for an incubation time of 24 h (experiment, Figure 2B, left) reveal that galvanic displacement results in uniform coverage of silver across the entire surface area of the disk. As previously mentioned, the SEM images reveal key differences in morphology between the control and experimental conditions. The SEM image of the Cu–PLA disks (Figure 2A, right) reveals heterogeneous spotting of copper, which has been brought to the surface via polishing (middle-top). The SEM image of the Ag–Cu–PLA disks (0.1 M AgNO<sub>3</sub>, 24 h) (Figure 2B, right) reveals silver structures with distinct polyhedral, fibrous, and branched morphologies. EDS point spectra were used to confirm the elemental composition of the Cu–PLA and Ag–Cu–PLA disks. The EDS spectra is represented as X-ray counts vs

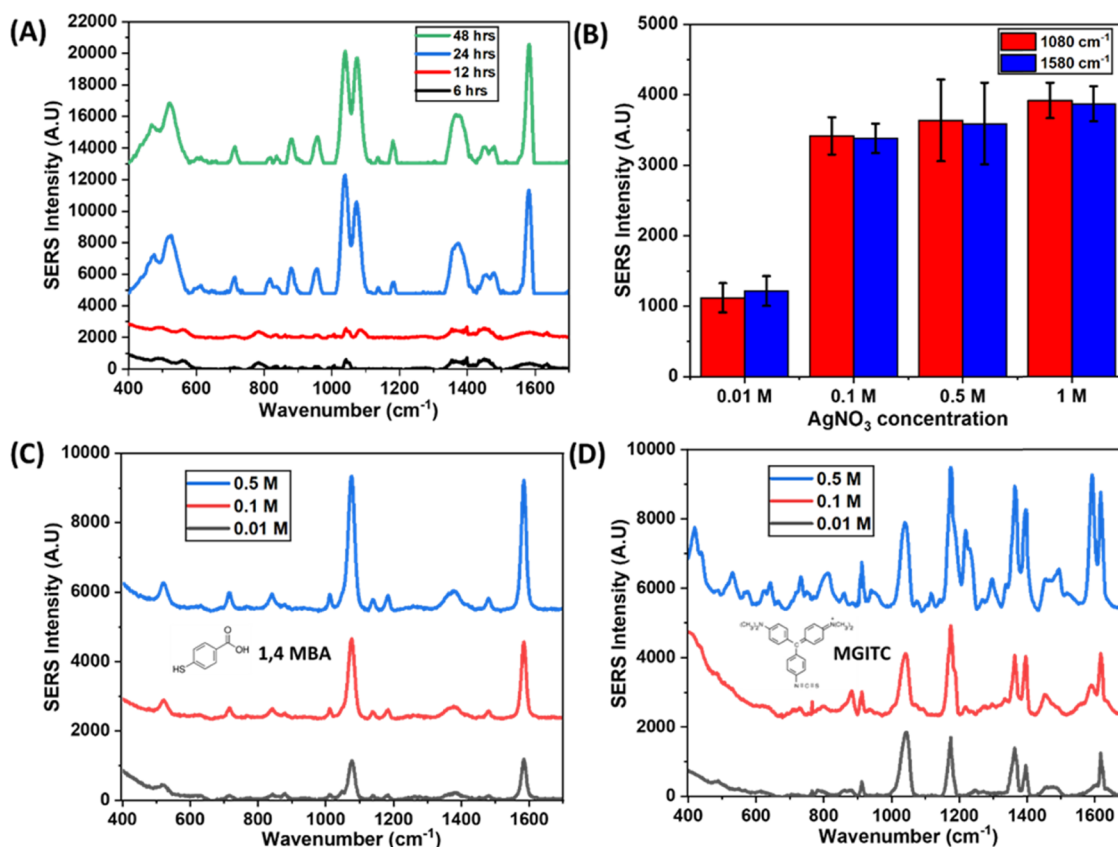


**Figure 4.** (A) SERS spectra observed for  $10^{-4}$  MBA deposited onto the Cu–PLA disks treated with 0.01 M  $\text{AgNO}_3$ , across various incubation times (6–48 h). (B) Measured SERS peak intensities for MBA ( $10^{-6}$  M) peaks present at 1080 and 1580  $\text{cm}^{-1}$ , all substrates were incubated with  $\text{AgNO}_3$  for 24 h. (C, D) SERS spectra comparing the intensities of vibrational modes of  $10^{-6}$  M MBA (C) at 1080 and 1580  $\text{cm}^{-1}$  and  $10^{-4}$  M MGITC (D) at 913, 1176, 1368, 1394, and 1614  $\text{cm}^{-1}$ . The SERS peak intensities show an increasing trend with an increase in  $\text{AgNO}_3$  concentrations. Peak intensities for MBA are differentiable for the tested  $\text{AgNO}_3$  concentrations when compared with MGITC. Spectra are baseline-corrected and background-subtracted from the SERS collected from the blank disks.

energy (keV) are displayed in Figure 2C–C1,C2. Copper peaks present at 1, 8, and 9 keV represent the highest densities (92.8%) within the control sample (Figure 2A), in addition to a small amount (<2%) of carbon and oxygen (Figure 2C–C1). Silver peaks are present at 3–3.5 keV representing the highest densities (79%) within the Ag–Cu–PLA disks. Copper (1.1%), carbon (2.6%), and oxygen (3.5%) make up the rest of the sample (Figure 2C–C2). Additionally, as the samples were sputter-coated with platinum (Pt) and palladium (Pd) to improve SEM images, those peaks can be observed too. Analysis of the EDS elemental mapping was carried out to determine the true spatial distribution of all constitutive elements selected within an area of interest (Figure 2B, red box). Elemental mapping of a polyhedral silver crystal and adjoining areas (Figure 2D–D1–D4) further confirms the successful galvanic displacement reaction with silver (D2) being interspersed over copper (D1). Carbon (D3) and oxygen (D4) are present along the peripheries of the silver structure indicating the presence of the polymeric PLA matrix.

Furthermore, the success of the galvanic displacement was confirmed by performing absorbance scans of the  $\text{Cu}^{2+}$  ions in solution, which causes it to turn blue during and after the completion of the galvanic displacement. Greater generation of the copper cation occurs with increased  $\text{AgNO}_3$  concentration and incubation times. The absorbance scan revealed broad absorption at 808 and 972 nm (Figure 3A). At 808 nm (Figure 3B) and 972 nm (Figure 3C), absorbance values for  $\text{AgNO}_3$

concentrations of 0.01 and 0.1 M are quite similar for displacement times of 6 and 12 h. At 24 and 48 h, a clear increase in absorbance values is seen with an increase in the concentration of  $\text{AgNO}_3$ . Additionally, for lower concentrations of 0.001 and 0.01 M, a plateauing of absorbance can be seen starting at 24 h. These observations further support the increase in Ag coverage on the Cu–PLA surface, which proceeds through simultaneous reactions, i.e., oxidation of Cu and reduction of Ag.

#### Comparing the SERS between Ag–Cu–PLA Disks Fabricated Using Different Concentrations of $\text{AgNO}_3$ .

The goal of this study was to investigate the feasibility of this proposed SERS substrate to detect molecules of interest (e.g., environmental contaminants such as CMIT) with high sensitivity. As mentioned in the Materials and Methods section, two common Raman reporters, MBA and MGITC, were used to demonstrate and evaluate the ability of the Ag–Cu–PLA substrates to produce enhancement effects. Both the Cu–PLA and Ag–Cu–PLA disks were initially submerged in an MBA solution ( $10^{-4}$  M) for a period of 24 h. Raman interrogation of the Cu–PLA control disks revealed that there was no SERS activity observed when submerged in either water or MBA. However, with Ag–Cu–PLA, some enhancement is seen when probing water, indicating that the galvanic displacement process results in the production of limited background SERS signals (Figure S1, SI). Initially, it was thought that the signals would interfere with chemical analyses,

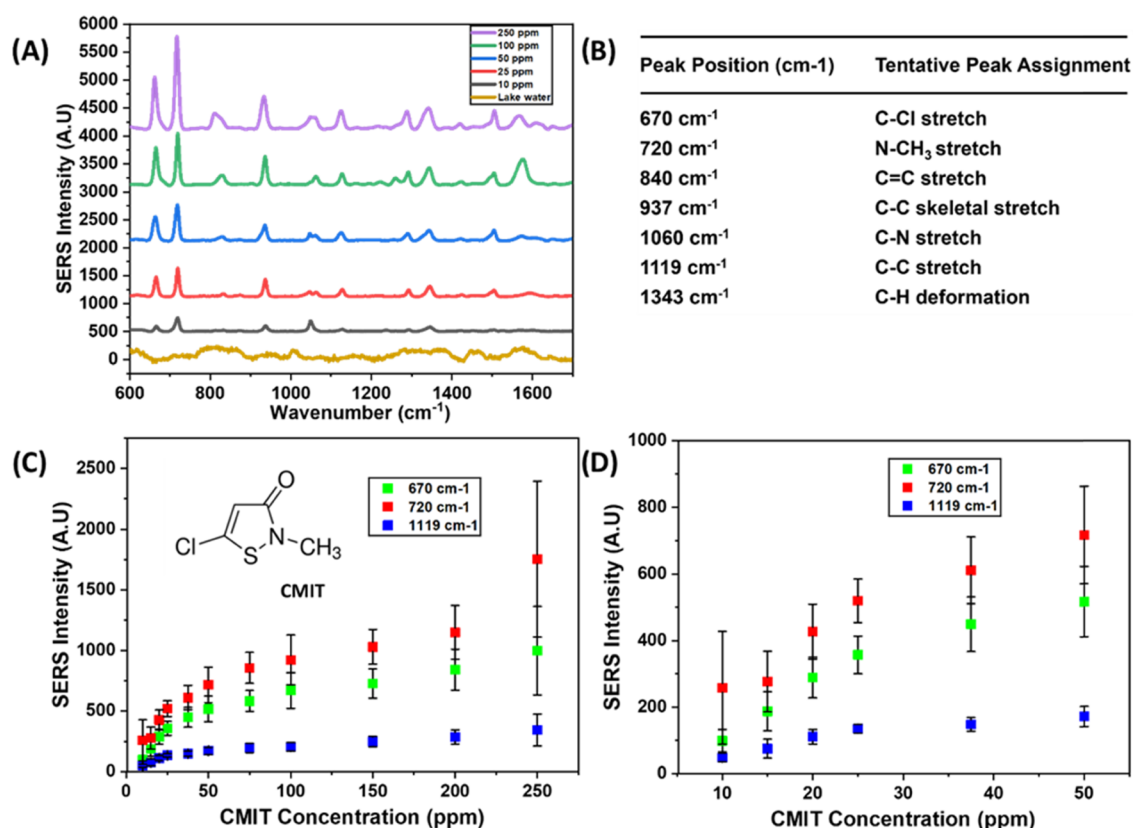


**Figure 5.** (A) SERS spectra for the determination of environmental contaminant CMIT spiked in simulated lake water samples. Concentrations of CMIT ranged from the lowest at 10 ppm to the highest at 250 ppm. (B) Tentative peak assignments representative of CMIT SERS vibrational modes observed on Ag–Cu–PLA substrates (right). (C) Vibrational modes at 670, 720, and 1119 cm<sup>-1</sup> were used to establish concentration dependence relationships for the assayed concentrations. Plateauing of SERS intensities is observed as higher concentrations of CMIT are reached. (D) SERS intensities at lower CMIT concentrations (10–50 ppm) are shown. Scatter plots represent mean ( $n = 3$ ) and error bars represent standard deviation.

but this was not so. Due to limited scattering observed from the substrate, 3D printed PLA matrices are an ideal candidate as substrates for Raman/SERS analysis applications.

To ascertain the optimal concentration of AgNO<sub>3</sub> and the incubation time for generation of high-performance SERS, the thin-film silver structure following experimental conditions was evaluated: AgNO<sub>3</sub> concentrations of 0.001 M were evaluated for incubation times ranging from 6 to 48 h. The resultant Ag–Cu–PLA substrates were immersed in MBA (10<sup>-4</sup> M) solutions for 24 h and the SERS readings were recorded and compared. It must be noted that the MBA incubation time was kept constant at 24 h. At the lowest AgNO<sub>3</sub> concentration, no SERS activity was observed (Figure S2, SI). However, when using the next highest AgNO<sub>3</sub> concentration (0.01 M), the SERS two vibrational peaks for MBA became evident after 24 h incubation. Peaks at 1080 cm<sup>-1</sup> (phenyl ring breathing and C–H in-plane bending) and 1580 cm<sup>-1</sup> (phenyl ring stretching) associated with MBA were used to assess SERS performance. Further examination of the SERS data revealed that the 1080 cm<sup>-1</sup> peak begins to appear after 12 h incubation, while the 1580 cm<sup>-1</sup> peak only appears after 24 h. The 24 h incubation period seemed appropriate with respect to bulk manufacturing of Cu–PLA substrates, going forward, especially when considering their perspective on field applications for environmental analysis (Figure 4A).

MBA (10<sup>-6</sup> M) was then incubated for 24 h with different Ag–Cu–PLA disks, and the two main characteristic peaks associated with MBA vibrational modes at 1080 and 1580

cm<sup>-1</sup> were measured. The intensities of both vibrational modes increased as the concentration of AgNO<sub>3</sub> used was increased until a plateau in signal intensity occurred at ~0.1 M AgNO<sub>3</sub> (Figure 4B).

With the aim of creating a SERS substrate capable for diverse analytes, three concentrations of AgNO<sub>3</sub> (0.01, 0.1, 0.5 M) were tested with 10<sup>-6</sup> M MBA (Figure 4C) and 10<sup>-4</sup> M MGITC (Figure 4D). The disks were incubated using the previously optimized incubation time of 24 h. In addition to observing the MBA modes, the prominent characteristic bands for MGITC are present at 914, 1171, and 1368 cm<sup>-1</sup>; these peaks can be attributed to the ring breathing, in-plane C–H bending, and in-plane N–phenyl stretching vibration, respectively.

Statistical analysis on peak intensities revealed no significant difference at concentrations of 0.1 and 0.5 M for the vibrational modes of MBA (Table S1, SI). Serial dilution experiments revealed that MBA could be detected at the picomolar level when substrates were prepared using the 0.1 M AgNO<sub>3</sub> concentration with 24 h incubation time (Figure S3A, SI).

The multiplexing abilities of the Ag–Cu–PLA substrates (i.e., the ability to detect multiple analytes simultaneously on a single substrate) were briefly explored. Equal volumes (2 mL) of 10<sup>-6</sup> M MBA and 10<sup>-4</sup> M MGITC were mixed, and the SERS spectra were collected, revealing visible vibrational modes of both the Raman analytes. The characteristic vibrational modes of MBA at 1080 and 1580 cm<sup>-1</sup> and

MGITC at 1171 and 1368  $\text{cm}^{-1}$  are visible on the SERS substrates synthesized using  $\text{AgNO}_3$  concentrations of 0.1 and 0.5 M. SERS activity was visibly absent at 0.01 M (Figure S3B, SI). These results indicate prospective opportunities for SERS multiplexed analysis on the substrates. Improvement in multiplexing is possible through modifications to the substrate with linkers to attract molecules with similar behavior and normalization of adsorption potentials of the different analytes.<sup>43,44</sup>

Spectroscopic evaluation of the substrates reveals that the SERS enhancement generally plateaus at higher concentrations. The 24 h test case with 0.1 M  $\text{AgNO}_3$  was further scrutinized to confirm the reproducibility of the 3D printed substrate. The widespread application of SERS and its translation into real-world applications has traditionally been limited due to signal reproducibility issues, so we measured the variance in signal associated with our best-performing Ag–Cu–PLA disk. The relative standard deviation (RSD) of the previously established MBA (1080  $\text{cm}^{-1}$ ) and MGITC peaks (1174  $\text{cm}^{-1}$ ) was evaluated to confirm the reproducibility of the SERS signal. The analyte-dependent RSD values measured across 20 spots spanning an area of  $2500 \times 2500 \mu\text{m}^2$  were found to be 18.36% for MGITC (Figure S4A, SI) and 16.98% for MBA (Figure S4B, SI). Furthermore, batch-to-batch reproducibility was confirmed by analyzing SERS intensity across 20 spots spanning  $2500 \times 2500 \mu\text{m}^2$  over 3 different preparations (0.1 M  $\text{AgNO}_3$ , 24 h) of discs. This time, SERS intensities of MBA at 1580  $\text{cm}^{-1}$  showed RSD values between 11 and 15% for each substrate (Figure S5B1–B3, SI), which means that there was <5% variation in RSD between replicate substrates. This fits well within the benchmark standard of RSD <20%, thus ascertaining the reproducibility of the 3D printed SERS substrates.<sup>45</sup> Twenty spectra are taken from random locations across the entirety of the substrate. However, Figure S6 has been included to show the variation in the signal observed across 100 MBA ( $10^{-4}$  M) spectra taken from a localized region. This reveals relatively homogeneous Raman intensities across the Ag–Cu–PLA discs (Figure S6A,B, SI).

**SERS Detection of Environmental Contaminant CMIT.** SERS analysis has emerged as an extremely promising solution for in situ in-field detection of environmental contaminants in food and water.<sup>46–48</sup> 5-Chloro-2-methyl-4-isothiazolin-3-one (CMIT) belonging to the isothiazolinones family is a highly deleterious chemical agent, with reports suggesting that CMIT is toxic toward animals.<sup>49–51</sup> Health issues in humans range from skin irritation and sensitization risks to interstitial lung injury and pulmonary dysfunction.<sup>52–55</sup> Additionally, it has been discovered that CMIT leaches into aquatic ecosystems and can be found in industrial wastewater liberated during the production and processing of personal care products and cleaning agents such as disinfectants.<sup>56–58</sup> Additionally, it is also a popular biocide used in fracking chemical cocktails further necessitating its regulated detection.<sup>59</sup> To demonstrate the practical utility of the Ag–Cu–PLA substrate, we utilized the systemically optimized substrate for the analysis of environmentally relevant concentrations of CMIT spiked in simulated lake water using SERS. We opted to use simulated lake water to observe any interferences caused by the presence of ions. Observation of the SERS spectra revealed a concentration-dependent increase in the vibrational modes (peak heights) for CMIT concentrations across a dynamic range of 10–250 ppm. (Figure 5A). SERS peaks are observed (Figure 5B) at 670, 720, and 1119  $\text{cm}^{-1}$ ; these have been

tentatively assigned to C–Cl stretch, N–CH<sub>3</sub> stretch, and C–C stretch vibrational modes.<sup>60</sup> Apparent saturation of SERS intensity is observed after 100 ppm along with an increase in the standard deviation of the replicate samples. The saturation at the higher concentrations of CMIT gives an overall sigmoidal-like fit for the concentration curve (Figure 5C). At the lower concentrations between 10 and 50 ppm, peak intensities at 1119  $\text{cm}^{-1}$  could be used for quantification to delineate low toxic concentrations of CMIT due to the relatively small standard deviations compared to vibrational modes at 670 and 720  $\text{cm}^{-1}$  (Figure 5D). Our limit of detection works out to 5.52 ppm when calculated with the vibrational mode of 670  $\text{cm}^{-1}$  (Figure S7). This compares favorably with studies utilizing chromatography methods such as HPLC/MS<sup>61,62</sup> and is additionally in line with the regulatory limits for safe exposure set forth by the European Union and the FDA.<sup>63</sup> Ag–Cu–PLA disks can thus quantitatively differentiate between CMIT concentrations spiked into the simulated lake water samples.

## CONCLUSIONS AND FUTURE WORK

3D printing has become increasingly more cost effective and accessible in recent years. The availability and broad range of printers and printing techniques mean that laboratories can now rapidly generate prototypes, equipment, and instrumentation to aid research. To satisfy the growing demand for plastic properties, manufacturers have expanded their range of polymer filaments and resins. In this work, we opted to use a copper-embedded PLA filament, which has multiple advantages when applied to the formation of SERS-active substrates. First, interrogation of the PLA using Raman spectroscopy revealed minimal background peak contributions making it more straightforward to resolve peaks from analytes deposited onto the substrates; second, the homogeneous incorporation of copper into the PLA enabled the rapid generation of SERS-active thin films using facile galvanic displacement reactions. The morphology of silver structures deposited onto the Cu–PLA disks was demonstrated to have a dependence on  $\text{AgNO}_3$  concentration. Additionally, standard Raman reporters such as MBA and MGITC were used to demonstrate optimal SERS performance at 24 h following incubation of Cu–PLA disks in  $\text{AgNO}_3$  solutions. Using the genotoxic isothiazolinone CMIT as our model analyte, we were able to demonstrate the analytical feasibility of our substrate. We were successfully able to detect CMIT at relevant toxic levels between 10 and 250 ppm, as established by regulatory agencies. To our knowledge, this is the first example of a 3D printed substrate being used to produce a template for the formation of a SERS-active silver thin film. Preparation of the substrates using the method we have described makes the SERS technique more accessible to research groups as it foregoes complex and expensive processes such as lithography. As such, it presents itself as a facile, rapid, low-cost option for the future development of high-performing SERS-active substrates. While several methods have already been established as affordable and high throughput for the fabrication of SERS-active substrates,<sup>7,9–12</sup> FDM-based 3D printing has the potential to craft distinct geometries at high resolutions through concise control of process parameters. The increasing resolution of FDM 3D printers means that the promise of readily available submicron scale printing is becoming more likely. This twined with the expanding list of metal-doped filaments will make the refinement of SERS-active

thin-film substrate properties possible. We foresee that these SERS platforms can function as standalone analytical substrates or could be integrated into other microfluidic-based devices, opening avenues for further investigations into effects of parameters such as mixing times, scattering cross sections, and temperature on SERS activity. Furthermore, the combination of rapid-large batch production capabilities of 3D printing and expansion of affordable, small form factor Raman spectrometers present exciting avenues for the growth of on-site SERS analysis. While we have demonstrated the feasibility of our substrates toward the detection of genotoxic analytes, we expect that SERS sensors fabricated using a combination of 3D printing and galvanic displacement can be applied to the further detection of other environmental contaminants and for biomedical applications including point-of-care diagnostics.<sup>64</sup>

## MATERIALS AND METHODS

**Chemicals.** Silver nitrate ( $\text{AgNO}_3$ , 99.8%), calcium chloride ( $\text{CaCl}_2$ , 99.8%), magnesium chloride ( $\text{MgCl}_2$ , >99.0%), sodium chloride ( $\text{NaCl}$ , >99.0%), potassium chloride ( $\text{KCl}$ , >99.0%), and magnesium sulfate ( $\text{MgSO}_4$ , >99.0%) were purchased from Sigma-Aldrich (MO). Malachite green isothiocyanate (MGITC, >98%) and 1,4-mercaptobenzoic acid (MBA, >99%) were purchased from Thermo Scientific (Waltham, MA). 5-Chloro-2-methyl-2*H*-isothiazolin-3-one/2-methyl-2*H*-isothiazol-3-one (CMIT, 14% aqueous solution) was purchased from Santa Cruz Biotechnology (Dallas, TX). Cu-PLA 3D printing filament (1.75 mm) was purchased from Protopasta (Vancouver, WA).

**3D Printing and Galvanic Displacement.** Cu-PLA disks (8 mm diameter  $\times$  1 mm thick) were printed using a Prusa i3 MK3S printer (Prusa Research, Czech Republic). Fusion 360 was used to design the disks, after which the design was converted to an .stl format ready for slicing. The proprietary PrusaSlicer software converts the .stl file into G-code instructions readable by the 3D printer. The following settings were used to slice the disks: object infill 100%; layer height 0.1 mm; print speed 100 mm/s; plastic filament diameter 1.75 mm; extrusion temperature 210 °C; and build plate temperature 60 °C. Silver nitrate solutions were prepared to concentrations of 0.001, 0.01, 0.1, 0.5, and 1 M. As Cu-PLA disks were immersed in 4 mL of silver nitrate solution for 6, 12, 24, and 48 h to produce Ag-Cu-PLA disks. Disks were rinsed using copious amounts of DI water, dried at 30 °C, and stored in a food dehydrator styled desiccator containing silica gel particles until needed. 3D printed discs were printed in batches of 10 and were stored up to a period of 14 days.

**Characterization.** The extinction spectra of copper ion solution ( $\text{Cu}^{2+}$ ) displaced from the composite 3D printed disks were measured using a Tecan Infinite 200 Pro microplate reader across a wavelength range of 400–1000 nm. The morphology (size and shape) of silver microstructures on Ag-Cu-PLA disks was investigated using a scanning electron microscope (SEM, JEOL JSM-7500F) equipped with a secondary electron image detector operating at 15 kV under a high vacuum. The control Cu-PLA disks (no silver) were polished using silicon carbide sandpaper (1500 grit) to enable better visualization of copper. An energy-dispersive X-ray spectroscopy system (EDS) equipped with the INCA analysis software was used to measure the elemental composition of silver microstructures formed because of the galvanic displacement process.

**Sample Preparation and SERS Measurements.** All analyte solutions of target concentrations were prepared in water (DI or simulated lake water). An ionic solution of simulated lake water was prepared using the following salt concentrations: 0.5 mM  $\text{CaCl}_2$ , 0.2 mM  $\text{MgCl}_2$ , 0.3 mM  $\text{NaCl}$ , 0.4 mM  $\text{KCl}$ , and 0.2 mM  $\text{MgSO}_4$  in 100 mL of DI water, according to a published protocol.<sup>65</sup> Ag-Cu-PLA disks were immersed in analyte solutions for 24 h, prior to SERS measurements being taken, to allow for maximum interaction between the Ag-Cu-PLA substrate and the analyte. MBA readings used in initial SERS measurements and the optimization of the substrates were performed using a Wasatch fiber-optic Raman setup (785 nm, 1 s integration time, 200–2700  $\text{cm}^{-1}$ , and 50 mW laser power). Raman spectra of CMIT were collected using a DXR Raman confocal microscope with a 780 nm wavelength and 24 mW diode laser as an illumination source. The magnification and numerical aperture of the objective were 10 $\times$  and 0.25, respectively. The spectra were collected across a wavelength range of 400–1800  $\text{cm}^{-1}$  with an exposure time of 1 s and a spectral resolution of 3.7  $\text{cm}^{-1}$ . While the portable systems established the presence of SERS enhancement, the desktop Raman microscope allowed for finer resolution of signal characteristics emanating from the thin-film silver substrates thus aiding substrate characterization. All spectra were baseline-corrected prior to analysis using an asymmetric least-squares method applied in MATLAB.<sup>66</sup>

**Image Analysis.** Particle tracking was used on SEM images to determine the area occupied by silver deposits. This analysis was performed using NIH ImageJ1.51J8. An average of 5 spots with individual areas 600  $\times$  600  $\mu\text{m}^2$  was analyzed for each of the deposition experimental conditions. Image pixel size was then calibrated by identifying the known distance and unit of length (scale bar on the image). Default local thresholding was used for the 8-bit binary image. The default watershed algorithm within ImageJ was used to segment and separate overlapping, closely packed crystals: 100  $\mu\text{m}^2$  was selected as the minimum area occupied by the silver deposits to be counted. Particle area and % silver coverage were calculated using this method.

## ASSOCIATED CONTENT

### Supporting Information

The Supporting Information is available free of charge at <https://pubs.acs.org/doi/10.1021/acsomega.1c05707>.

SERS spectra collected from blank Cu-PLA discs; SERS spectra of 10<sup>-4</sup> M MBA incubated on 0.001 M Ag-Cu-PLA disc; single-factor ANOVA comparing mean peak intensities of MBA; SERS intensity observed on Ag-Cu-PLA disks for MBA; multiplexed SERS detection of MBA and MGITC on Ag-Cu-PLA disks; boxplots demonstrating the reproducibility of SERS signal using MBA and MGITC; average SERS signal across 20 spots across an area of 2500  $\times$  2500  $\mu\text{m}^2$  demonstrating batch to batch reproducibility; heat map and Waterfall plot of SERS intensities across 100 spots collected on the Ag-Cu-PLA discs across the 2500  $\times$  2500  $\mu\text{m}^2$  and linear calibration curve of SERS intensity (0–50 ppm) to determine the limit of detection of CMIT (PDF)



## AUTHOR INFORMATION

### Corresponding Author

Samuel Mabbott – Department of Biomedical Engineering, Texas A&M University, College Station, Texas 77843, United States; Center for Remote Health Technologies & Systems, Texas A&M Engineering Experiment Station, College Station, Texas 77840-3006, United States; [orcid.org/0000-0003-4926-5467](https://orcid.org/0000-0003-4926-5467); Email: [smabbott@tamu.edu](mailto:smabbott@tamu.edu)

### Authors

Siddhant Jaitpal – Department of Biomedical Engineering, Texas A&M University, College Station, Texas 77843, United States; Center for Remote Health Technologies & Systems, Texas A&M Engineering Experiment Station, College Station, Texas 77840-3006, United States; [orcid.org/0000-0001-5780-7225](https://orcid.org/0000-0001-5780-7225)

Suhash Reddy Chavva – Department of Biomedical Engineering, Texas A&M University, College Station, Texas 77843, United States; Center for Remote Health Technologies & Systems, Texas A&M Engineering Experiment Station, College Station, Texas 77840-3006, United States

Complete contact information is available at:

<https://pubs.acs.org/10.1021/acsomega.1c05707>

### Notes

The authors declare no competing financial interest.

## ACKNOWLEDGMENTS

This research was supported by start-up funds allocated to S.M. via TAMU and Texas Engineering Experiment Station. S.M., S.J., and S.R.C. would like to thank the college and the department for the support they have provided. The help and support of Dr. Yordanos Bisrat from TAMU Materials Characterization Facility and Dr. Stanislav Vitha from the TAMU Microscopy and Imaging Center is also acknowledged.

## REFERENCES

- (1) Sharma, B.; Frontiera, R. R.; Henry, A. I.; Ringe, E.; Van Duyne, R. P. SERS: Materials, applications, and the future. *Mater. Today* **2012**, *15*, 16–25.
- (2) Halvorson, R. A.; Vikesland, P. J. Surface-enhanced Raman spectroscopy (SERS) for environmental analyses. *Environ. Sci. Technol.* **2010**, *44*, 7749–7755.
- (3) Valley, N.; Greeneltch, N.; Van Duyne, R. P.; Schatz, G. C. A look at the origin and magnitude of the chemical contribution to the enhancement mechanism of surface-enhanced Raman spectroscopy (SERS): Theory and experiment. *J. Phys. Chem. Lett.* **2013**, *4*, 2599–2604.
- (4) Schatz, G. C.; Young, M. A.; Van Duyne, R. P. Electromagnetic Mechanism of SERS. In *Surface-Enhanced Raman Scattering Physics and Applications*, 1st ed.; Koelsch, H. J., Ed.; Academic Press: New York, 2006; pp 19–45.
- (5) Jeon, T. Y.; Kim, D.-J.; Park, S.-G.; Kim, S. H.; Kim, D. H. Nanostructured plasmonic substrates for use as SERS sensors. *Nano Convergence* **2016**, *3*, No. 18.
- (6) Mosier-Boss, P. A. Review of SERS substrates for chemical sensing. *Nanomaterials* **2017**, *7*, No. 142.
- (7) Sharma, B.; Cardinal, M. F.; Kleinman, S. L.; Greeneltch, N. G.; Frontiera, R. R.; Blaber, M. G.; Schatz, G. C.; Van Duyne, R. P. High-performance SERS substrates: Advances and challenges. *MRS Bull.* **2013**, *38*, 615–624.
- (8) Betz, J. F.; Wei, W. Y.; Cheng, Y.; White, I. M.; Rubloff, G. W. Simple SERS substrates: powerful, portable, and full of potential. *Phys. Chem. Chem. Phys.* **2014**, *16*, 2224–2239.
- (9) Xu, L.; Liu, H.; Zhou, H.; Hong, M. One-step fabrication of metal nanoparticles on polymer film by femtosecond LIPAA method for SERS detection. *Talanta* **2021**, *228*, No. 122204.
- (10) Zhou, N.; Meng, G.; Huang, Z.; Ke, Y.; Zhou, Q.; Hu, X. A flexible transparent Ag-NC@PE film as a cut-and-paste SERS substrate for rapid *in situ* detection of organic pollutants. *Analyst* **2016**, *141*, 5864–5869.
- (11) Chen, B.; Meng, G.; Huang, Q.; Huang, Z.; Xu, Q.; Zhu, C.; Qian, Y.; Ding, Y. Green Synthesis of Large-Scale Highly Ordered Core@Shell Nanoporous Au@Ag Nanorod Arrays as Sensitive and Reproducible 3D SERS Substrates. *ACS Appl. Mater. Interfaces* **2014**, *6*, 15667–15675.
- (12) Xu, K.; Zhou, R.; Takei, K.; Hong, M. Toward flexible surface-enhanced Raman scattering (SERS) sensors for point-of-care diagnostics. *Adv. Sci.* **2019**, *6*, No. 1900925.
- (13) Cardoso, R. M.; Mendonça, D. M.; Silva, W. P.; Silva, M. N.; Nossol, E.; da Silva, R. A.; Richter, E. M.; Muñoz, R. A. 3D printing for electroanalysis: from multiuse electrochemical cells to sensors. *Anal. Chim. Acta* **2018**, *1033*, 49–57.
- (14) Palenzuela, C. L. M.; Pumera, M. (Bio) Analytical chemistry enabled by 3D printing: Sensors and biosensors. *TrAC, Trends Anal. Chem.* **2018**, *103*, 110–118.
- (15) Gross, B.; Lockwood, S. Y.; Spence, D. M. Recent advances in analytical chemistry by 3D printing. *Anal. Chem.* **2017**, *89*, 57–70.
- (16) Xu, W.; Jambhulkar, S.; Ravichandran, D.; Zhu, Y.; Kakarla, M.; Nian, Q.; Azeredo, B.; Chen, X.; Jin, K.; Vernon, B.; Lott, D. G.; et al. 3D Printing-Enabled Nanoparticle Alignment: A Review of Mechanisms and Applications. *Small* **2021**, *17*, No. 2100817.
- (17) Flowers, P. F.; Reyes, C.; Ye, S.; Kim, M. J.; Wiley, B. J. 3D printing electronic components and circuits with conductive thermo-plastic filament. *Addit. Manuf.* **2017**, *18*, 156–163.
- (18) Sochol, R. D.; Sweet, E.; Glick, C. C.; Wu, S. Y.; Yang, C.; Restaino, M.; Lin, L. 3D printed microfluidics and microelectronics. *Microelectron. Eng.* **2018**, *189*, 52–68.
- (19) Hwang, S.; Reyes, E. I.; Moon, K. S.; Rumpf, R. C.; Kim, N. S. Thermo-mechanical characterization of metal/polymer composite filaments and printing parameter study for fused deposition modeling in the 3D printing process. *J. Electron. Mater.* **2015**, *44*, 771–777.
- (20) Angel, K.; Tsang, H. H.; Bedair, S. S.; Smith, G. L.; Lazarus, N. Selective electroplating of 3D printed parts. *Addit. Manuf.* **2018**, *20*, 164–172.
- (21) Djokić, S. S. Electroless Deposition of Metals and Alloys. In *Modern Aspects of Electrochemistry*, 35th ed.; Conway, B. E.; White, R. E., Eds.; Springer: Boston, MA, 2002; pp 51–133.
- (22) Avizienis, A. V.; Martin-Olmos, C.; Sillin, H. O.; Aono, M.; Gimzewski, J. K.; Stieg, A. Z. Morphological transitions from dendrites to nanowires in the electroless deposition of silver. *Cryst. Growth Des.* **2013**, *13*, 465–469.
- (23) Coluccio, M. L.; Das, G.; Mearini, F.; Gentile, F.; Pujia, A.; Bava, L.; Talerico, R.; Candeloro, P.; Liberale, C.; De Angelis, F.; Di Fabrizio, E. Silver-based surface enhanced Raman scattering (SERS) substrate fabrication using nanolithography and site selective electroless deposition. *Microelectron. Eng.* **2009**, *86*, 1085–1088.
- (24) Mabbott, S.; Xu, Y.; Goodacre, R. Objective assessment of SERS thin films: comparison of silver on copper via galvanic displacement with commercially available fabricated substrates. *Anal. Methods* **2017**, *9*, 4783–4789.
- (25) Volochanskyi, O.; Švecová, M.; Bartůněk, V.; Prokopec, V. Electroless deposition via galvanic displacement as a simple way for the preparation of silver, gold, and copper SERS-active substrates. *Colloids Surf., A* **2021**, *616*, No. 126310.
- (26) Ahn, S. H.; Montero, M.; Odell, D.; Roundy, S.; Wright, P. K. Anisotropic material properties of fused deposition modeling ABS. *Rapid Prototyping J.* **2002**, *8*, 248–257.
- (27) Patton, M. V.; Ryan, P.; Calascione, T.; Fischer, N.; Morgenstern, A.; Stenger, N.; Nelson-Cheeseman, B. B. Manipulating magnetic anisotropy in fused filament fabricated parts via macroscopic shape, mesoscopic infill orientation, and infill percentage. *Addit. Manuf.* **2019**, *27*, 482–488.

- (28) Prajapati, H.; Ravoori, D.; Woods, R. L.; Jain, A. Measurement of anisotropic thermal conductivity and inter-layer thermal contact resistance in polymer fused deposition modeling (FDM). *Addit. Manuf.* **2018**, *21*, 84–90.
- (29) Zhang, J.; Yang, B.; Fu, F.; You, F.; Dong, X.; Dai, M. Resistivity and its anisotropy characterization of 3D-printed acrylonitrile butadiene styrene copolymer (ABS)/carbon black (CB) composites. *Appl. Sci.* **2017**, *7*, No. 20.
- (30) Reguera, J.; Langer, J.; de Aberasturi, D. J.; Liz-Marzán, L. M. Anisotropic metal nanoparticles for surface enhanced Raman scattering. *Chem. Soc. Rev.* **2017**, *46*, 3866–3885.
- (31) Michieli, N.; Pilot, R.; Russo, V.; Scian, C.; Todescato, F.; Signorini, R.; Agnoli, S.; Cesca, T.; Bozio, R.; Mattei, G. Oxidation effects on the SERS response of silver nanoprisms arrays. *RSC Adv.* **2017**, *7*, 369–378.
- (32) Chen, L. X.; Li, D. W.; Qu, L. L.; Li, Y. T.; Long, Y. T. SERS sensing of sulfide based on the sulfidation of silver nanoparticles. *Anal. Methods* **2013**, *5*, 6579–6582.
- (33) Zhao, X.; Sakuma, K.; Yamaguchi, M.; Muraoka, M. Anisotropic surface-enhanced Raman scattering in shape-controlled Ag microcoils. *Mater. Lett.* **2021**, *300*, No. 130178.
- (34) Lin, Y. W.; Tang, C. Electrochemical synthesis and deposition of surface-enhanced Raman scattering-active silver microstructures on a screen-printed carbon electrode. *J. Phys. Chem. C* **2015**, *119*, 24865–24874.
- (35) Chen, X.; Cui, C. H.; Guo, Z.; Liu, J. H.; Huang, X. J.; Yu, S. H. Unique heterogeneous silver–copper dendrites with a trace amount of uniformly distributed elemental Cu and their enhanced SERS properties. *Small* **2011**, *7*, 858–863.
- (36) Gutiérrez, A.; Carraro, C.; Maboudian, R. Silver dendrites from galvanic displacement on commercial aluminum foil as an effective SERS substrate. *J. Am. Chem. Soc.* **2010**, *132*, 1476–1477.
- (37) Jiang, Z.; Lin, Y.; Xie, Z. Structural investigations and growth mechanism of well-defined Ag dendrites prepared by conventional redox displacement. *Mater. Chem. Phys.* **2012**, *134*, 762–767.
- (38) Zhang, Y.; Sun, S.; Zhang, X.; Tang, L.; Song, X.; Yang, Z. Sulfate-ion-assisted galvanic replacement tuning of silver dendrites to highly branched chains for effective SERS. *Phys. Chem. Chem. Phys.* **2014**, *16*, 18918–18925.
- (39) Relinque, J. J.; de León, A. S.; Hernández-Saz, J.; García-Romero, M. G.; Navas-Martos, F. J.; Morales-Cid, G.; Molina, S. I. Development of surface-coated polylactic acid/polyhydroxyalkanoate (PLA/PHA) nanocomposites. *Polymers* **2019**, *11*, No. 400.
- (40) Ye, W.; Chen, Y.; Zhou, F.; Wang, C.; Li, Y. Fluoride-assisted galvanic replacement synthesis of Ag and Au dendrites on aluminum foil with enhanced SERS and catalytic activities. *J. Mater. Chem.* **2012**, *22*, 18327–18334.
- (41) Im, S. H.; Lee, Y. T.; Wiley, B.; Xia, Y. Large-scale synthesis of silver nanocubes: the role of hcl in promoting cube perfection and monodispersity. *Angew. Chem., Int. Ed.* **2005**, *44*, 2154–2157.
- (42) Wiley, B.; Herricks, T.; Sun, Y.; Xia, Y. Polyol synthesis of silver nanoparticles: use of chloride and oxygen to promote the formation of single-crystal, truncated cubes and tetrahedrons. *Nano Lett.* **2004**, *4*, 1733–1739.
- (43) Wang, C. M.; Roy, P. K.; Juluri, B. K.; Chattopadhyay, S. A SERS tattoo for in situ, ex situ, and multiplexed detection of toxic food additives. *Sens. Actuators, B* **2018**, *261*, 218–225.
- (44) Singh, J.; Manna, A. K.; Soni, R. K. Bifunctional Au–TiO<sub>2</sub> thin films with enhanced photocatalytic activity and SERS based multiplexed detection of organic pollutant. *J. Mater. Sci.: Mater. Electron.* **2019**, *30*, 16478–16493.
- (45) Zhang, B.; Wang, H.; Lu, L.; Ai, K.; Zhang, G.; Cheng, X. Large-Area Silver-Coated Silicon Nanowire Arrays for Molecular Sensing Using Surface-Enhanced Raman Spectroscopy. *Adv. Funct. Mater.* **2008**, *18*, 2348–2355.
- (46) Tang, J.; Chen, W.; Ju, H. Rapid detection of pesticide residues using a silver nanoparticles coated glass bead as nonplanar substrate for SERS sensing. *Sens. Actuators, B* **2019**, *287*, 576–583.
- (47) Sun, Z.; Du, J.; Jing, C. Recent progress in detection of mercury using surface enhanced Raman spectroscopy—A review. *J. Environ. Sci.* **2016**, *39*, 134–143.
- (48) Huang, C. C.; Cheng, C. Y.; Lai, Y. S. Paper based flexible surface enhanced Raman scattering platforms and their applications to food safety. *Trends Food Sci. Technol.* **2020**, *100*, 349–358.
- (49) Bruze, M.; Fregert, S.; Gruvberger, B.; Persson, K.; Dahlquist, I. Contact allergy to the active ingredients of Kathon CG. *Contact Dermatitis* **1987**, *16*, 183–188.
- (50) Botham, P. A.; Hilton, J.; Evans, C. D.; Lees, D.; Hall, T. J. Assessment of the relative skin sensitizing potency of 3 biocides using the murine local lymph node assay. *Contact Dermatitis* **1991**, *25*, 172–177.
- (51) Kim, Y.; Choi, J. Early life exposure of a biocide, CMIT/MIT causes metabolic toxicity via the O-GlcNAc transferase pathway in the nematode *C. elegans*. *Toxicol. Appl. Pharmacol.* **2019**, *376*, 1–8.
- (52) Herman, A.; Aerts, O.; de Montjoye, L.; Tromme, L.; Goossens, A.; Baeck, M. Isothiazolinone derivatives and allergic contact dermatitis: a review and update. *J. Eur. Acad. Dermatol. Venereol.* **2019**, *33*, 267–276.
- (53) Isaksson, M.; Gruvberger, B.; Bruze, M. Patch testing with serial dilutions of various isothiazolinones in patients hypersensitive to methylchloroisothiazolinone/methylisothiazolinone. *Contact Dermatitis* **2014**, *70*, 270–275.
- (54) Cho, H. J.; Lee, S. Y.; Park, D.; Ryu, S. H.; Yoon, J.; Jung, S.; Lee, E.; Yang, S. I.; Hong, S. J. Early-life exposure to humidifier disinfectant determines the prognosis of lung function in children. *BMC Pulm. Med.* **2019**, *19*, No. 261.
- (55) Lee, E.; Son, S. K.; Yoon, J.; Cho, H. J.; Yang, S. I.; Jung, S.; Do, K. H.; Cho, Y. A.; Lee, S. Y.; Park, D. U.; Hong, S. J. Two cases of chloromethylisothiazolinone and methylisothiazolinone-associated toxic lung injury. *J. Korean Med. Sci.* **2018**, *33*, No. 1107778.
- (56) Aerts, O.; Goossens, A.; Lambert, J.; Lepoittevin, J. P. Contact allergy caused by isothiazolinone derivatives: an overview of non-cosmetic and unusual cosmetic sources. *Eur. J. Dermatol.* **2017**, *27*, 115–122.
- (57) Friis, U. F.; Menné, T.; Flyvholm, M. A.; Bonde, J. P. E.; Lepoittevin, J. P.; Le Coz, C. J.; Johansen, J. D. Isothiazolinones in commercial products at Danish workplaces. *Contact Dermatitis* **2014**, *71*, 65–74.
- (58) Thomsen, A. V.; Schwensen, J. F.; Bossi, R.; Banerjee, P.; Giménez-Arnau, E.; Lepoittevin, J. P.; Lidén, C.; Uter, W.; White, I. R.; Johansen, J. D. Isothiazolinones are still widely used in paints purchased in five European countries: a follow-up study. *Contact Dermatitis* **2018**, *78*, 246–253.
- (59) Kahrilas, G. A.; Blotvogel, J.; Stewart, P. S.; Borch, T. Biocides in hydraulic fracturing fluids: a critical review of their usage, mobility, degradation, and toxicity. *Environ. Sci. Technol.* **2015**, *49*, 16–32.
- (60) Kang, T. H.; Jin, C. M.; Lee, S.; Choi, I. Dual Mode Rapid Plasmonic Detections of Chemical Disinfectants (CMIT/MIT) Using Target-Mediated Selective Aggregation of Gold Nanoparticles. *Anal. Chem.* **2020**, *92*, 4201–4208.
- (61) Heo, J. J.; Kim, U. J.; Oh, J. E. Simultaneous quantitative analysis of four isothiazolinones and 3-iodo-2-propynyl butyl carbamate in hygienic consumer products. *Environ. Eng. Res.* **2019**, *24*, 137–143.
- (62) Rosero-Moreano, M.; Canellas, E.; Nerin, C. Three-phase hollow-fiber liquid-phase microextraction combined with HPLC–UV for the determination of isothiazolinone biocides in adhesives used for food packaging materials. *J. Sep. Sci.* **2014**, *37*, 272–280.
- (63) Burnett, C. L.; Bergfeld, W. F.; Belsito, D. V.; Klaassen, C. D.; Marks, J. G.; Shank, R. C.; Slaga, T. J.; Snyder, P. W.; Andersen, F. A. Final report of the safety assessment of methylisothiazolinone. *Int. J. Toxicol.* **2010**, *29*, 187S–213S.
- (64) Langer, J.; Jimenez de Aberasturi, D.; Aizpurua, J.; Alvarez-Puebla, R. A.; Auguie, B.; Baumberg, J. J.; Bazan, G. C.; Bell, S. E.; Boisen, A.; Brolo, A. G.; Choo, J.; et al. Present and future of surface-enhanced Raman scattering. *ACS Nano* **2019**, *14*, 28–117.

(65) Sugiyama, M.; Wu, S.; Hosoda, K.; Mochizuki, A.; Hori, T. Method for the preparation of artificial lake and river waters. *Limnol. Oceanogr.: Methods* **2016**, *14*, 343–357.

(66) Eilers, P. H.; Boelens, H. F. Baseline correction with asymmetric least squares smoothing. *Leiden Univ. Med. Cent. Rep.* **2005**, *1*, No. 5.